INVESTIGATION INTO HIGH-TEMPERATURE CORROSION IN A LARGE-SCALE MUNICIPAL WASTE-TO-ENERGY PLANT

Awassada Phongphiphat[a1], Changkook Ryu[a2], Yao Bin Yang[a3], Karen N Finney[a]*, Adrian Leyland[b], Vida N Sharifi[a], Jim Swithenbank[a]

[a]Sheffield University Waste Incineration Centre (SUWIC), Department of Chemical and Process Engineering, University of Sheffield, Mappin Street, Sheffield, S1 3JD, UK

[b]Department of Engineering Materials, Sir Robert Hadfield Building, University of Sheffield, Mappin Street, Sheffield, S1 3JD, UK

*Corresponding author. Tel: +44-114-2227572, Fax: +44-114-2227501, Email: K.Finney@sheffield.ac.uk

ABSTRACT

High-temperature corrosion in the superheater of a large-scale waste-to-energy plant was investigated. A comparison of nickel-/iron-based alloys and austenitic stainless steel probes placed in the furnace demonstrated that temperature and particle deposition greatly influence corrosion. Nickel-based alloys performed better than the other metal alloys, though an aluminide coating further increased their corrosion resistance. Sacrificial baffles provided additional room for deposit accumulation, resulting in vigorous deposit-induced corrosion. Computational modelling (FLUENT code) was used to simulate flow characteristics and heat transfer. This study has shown that the use of aluminide coatings is a promising technique for minimising superheater corrosion in such facilities.

Keywords: alloys; metal coatings; modelling studies; SEM; XRD; high temperature corrosion.

---

[1] Present address: The Joint Graduate School of Energy and Environment, King Mongkut's University of Technology Thonburi, Bangmod, Tungkru, Bangkok, 10140, Thailand

[2] Present address: School of Mechanical Engineering, Sungkyunkwan University, Suwon, South Korea

[3] Present address: Biomass Power Ltd., Lichfield Road, Stafford, ST17 4BQ, UK

1. INTRODUCTION

A sustainable management strategy for municipal solid waste (MSW) includes reducing the amount of waste generated and reusing certain materials, as well as making use of recycling and energy recovery processes, followed by the environmentally-sound disposal of any residues. MSW consists of a putrescible fraction, along with paper, plastics, textiles, metals, glass and other miscellaneous materials. After recovering valuable recyclables by segregation, the waste can be thermo-chemically treated. Among the many technologies available for energy recovery, mass-burn incineration is well established. Coal-fired power stations have efficiencies in the region of 35%. While typical efficiencies for waste-to-energy (WTE) facilities are in the range of 25-30% for electricity generation only, when heat and power production are combined, much higher overall efficiencies can be achieved. Furthermore, more than two thirds of the carbon in MSW is greenhouse gas-neutral.

1.1 High Temperature Corrosion in Waste-To-Energy Facilities

High temperature corrosion of heat exchangers is one of the most important factors that limits the efficiency of various energy systems [1-4]. In combustion processes utilizing biomass or MSW, the steam temperatures are usually kept lower than 450°C to avoid corrosion problems [5]. Raising the steam temperature by an additional 50°C can result in significant increases in the corrosion rate in a biomass power plant [2,6]. Such problems become amplified by: (i) the use of fuels containing alkali metals, heavy metals, Cl and S; (ii) fluctuations in the flue gas flow; (iii) the high velocity, particle-bearing flue gas; and finally (iv) deposit (combustion residues) accumulation [3,5,7,8]. High temperature corrosion can be amplified by a range of factors. Problems related to flue gas fluctuations and particle trajectory, for example, can be predicted, controlled and prevented using computational fluid dynamics (CFD) modelling. This has proved to be an effective tool for simulating and optimising flow conditions, heat transfer and particle trajectories inside the furnace [8]. As stated above, overall efficiencies for WTE plants are relatively low, thus methods to prevent or control high temperature corrosion in such plants must be investigated in order to improve efficiencies.

Unfortunately, WTE facilities are more susceptible to severe corrosion than other types of energy systems due to the presence of deposits containing alkali and heavy metals (such as Na, K, Pb, Zn and Cd), as well as Cl and S. These elements originate in the fuel and lead to the formation of eutectic compounds with low

melting points [3,5,7-10]; fuel composition is the main factor determining high temperature corrosion in WTE plants. Liquid phase corrosion or hot corrosion is highly likely to take place on superheater tubes, resulting in high annual repair and replacement costs. Reliable and cost-effective methods to control corrosion in these plants must therefore be explored. One corrosion control method is the use of high-grade alloys, however, this is not generally cost-effective. Approaches that are more popular are to use coatings or sacrificial baffles. Aluminide coatings, which form a protective oxide layer of Al_2O_3, and chromized coatings (Cr_2O_3), have been found to be effective in minimising high temperature corrosion [11-13]. An aluminide coating on cheaper stainless steels may provide engineers with a high corrosion resistance material at an affordable price.

1.2 Aims and Objectives

The main objectives of this research were: (i) to investigate the corrosion behaviour of three high temperature super-alloys in a large-scale WTE plant; (ii) to evaluate the performance of aluminide coatings and sacrificial baffles in this facility; and (iii) to recommend appropriate techniques for corrosion minimisation in the superheater.

2. MATERIALS AND METHODS

2.1 The Waste-to-Energy Plant

This investigation was conducted at a large-scale WTE facility – a commercial mass-burn MSW incinerator. The waste, which is fed by ram feeders, undergoes combustion on the grate in the combustion chamber with primary air for about 60-80 minutes, at temperatures of 1000-1200°C. The temperature (over 800°C) and oxygen (over 10%dry) measurements acquired directly from the bed using a novel measuring technique showed very large fluctuations during combustion, due to the heterogeneous nature of the waste particles, solid particle mixing and the channelling of air through the waste particles. Secondary air is injected in the form of jets at each side-wall above the bed in order to aid turbulent mixing and supply additional oxygen to the combustion gases. Due to the furnace geometry and secondary air injection, the gas flow field has a high velocity (7-12 m/s) at over 1000°C, developed from above the bed to the exit of the radiation shaft and is thus likely to carry large amounts of particles to the heat exchangers. The gases pass through a pendant

superheater, a vaporiser, a multi-tubular heat exchanger and economisers for energy recovery. The gas temperature at the superheater inlet is about 800°C and drops to 230°C at the boiler exit. The gas then enters the air pollution control system. Here, injections of hydrated lime sorbents are used for the removal of acid gases and activated carbon is used to capture heavy metals and organic compounds. The amounts of lime and activated carbon injections are about 9 kg/ton-waste and 0.2 kg/ton-waste, respectively. The residual particulate matter is removed from the gas stream using bag/fabric filters. The temperatures at the economiser exit and at the fabric filter exit are about 135°C and 120°C, respectively. Figure 1 shows a schematic diagram of a typical WTE plant.
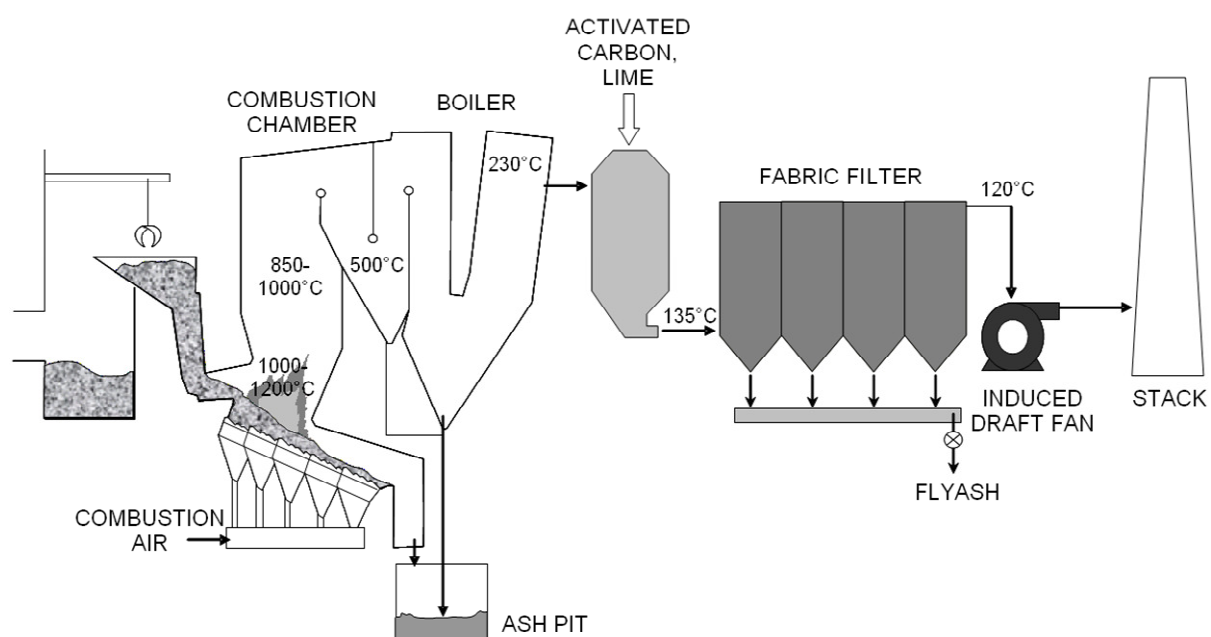
Figure 1. A schematic overview of a typical municipal solid waste (mass-burn) incineration process at an energy-from-waste facility.

2.2 Experimental Probe Fabrication and Placement

Two air cooled sampling probes, SP1 and SP2, were fabricated for this study. They were placed in the furnace, via existing viewing ports, for approximately 800 hours. A schematic diagram of the probe locations is presented in Figure 2. The main structure of the probes was made from a 1.5 m-long tube of Inconel 625 – a nickel-based alloy. This had an inner diameter of 1-inch (25.4 mm) and an outer diameter of 1.25 inches (31.75 mm), resulting in a wall thickness of 0.125 inches (3.175 mm). Three identical sets of alloys rings were welded onto the main tube at 0.59 m (wall-section), 0.87 m (mid-section) and 1.16 m (end-section) from the furnace wall. Each set of rings was composed of three individual rings made of 2 nickel-based alloys (alloy 59 and alloy 625) and an iron-based alloy (alloy 556).
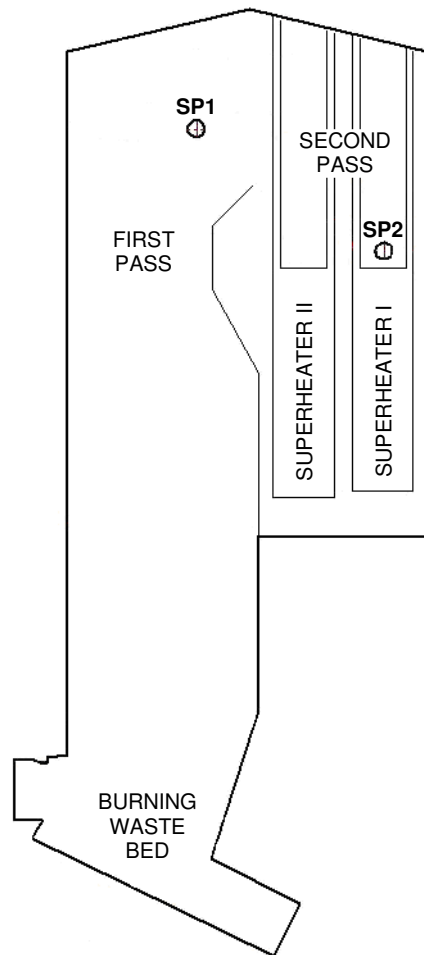
Figure 2. Schematic diagram of the furnace (side view) and the locations of the two sampling probes.

Triangular baffles made from stainless steel 316 sheets, with an angle of 45°, were welded at to the main tube at 0.42 m and 1.33 m from the wall according to the flow direction: on the bottom for SP1 and on the top for SP2. Four coupons of aluminide coated alloys (nickel-based alloy 59 and stainless steel 310), which were 2 mm thick, were also welded onto SP2. These were connected to the main tube at 0.72 m (wall-section) and 1.25 m (end-section) from the wall. The design of SP2 and its components are shown in Figure 3 and the chemical compositions of all these materials are presented in Table 1. The aluminide pack cementation coating process was conducted by the Advanced Material Research Institute, at Northumbria University, Newcastle, UK. Firstly, coupons were ground up to 600 SiC grit finish and then heated in a ceramic crucible packed with proprietary aluminising chemicals in the furnace. For the nickel alloy 59, the coupons were heated to a temperature of 1000°C and held for 5 hours. The aluminising mixture was composed of 15% Al, 3% NH_4Cl and 82% Al_2O_3, by weight. For stainless steel 310, the coupons were heated to a temperature of 850°C and held for 5 hours in an aluminising mixture composed of 4% Al, 2% $AlCl_3$ and 94% Al_2O_3, by weight.
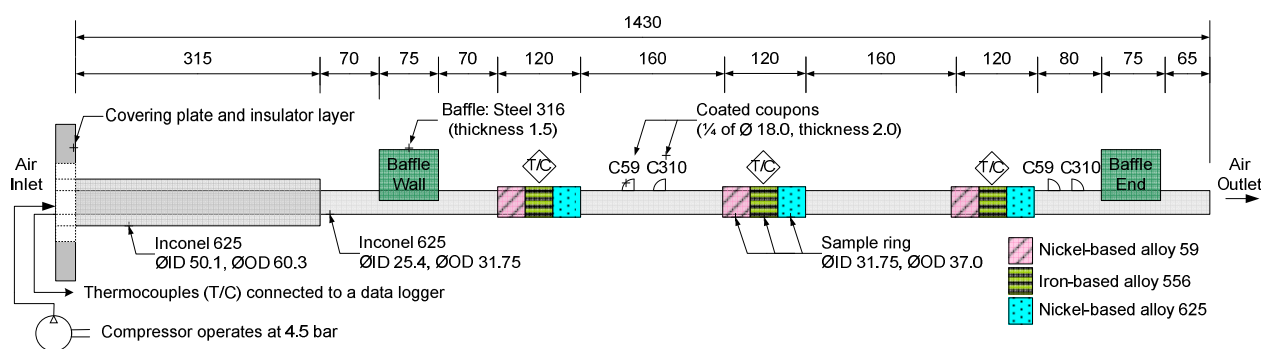
Figure 3. Schematic diagram of sampling probe 2 (SP2). All dimension measurements given in mm.

Alloy	Al	Co	Cr	Fe	Mn	Mo	Ni	Si	Others (>0.1%)
Ni-59	0.1-0.4	< 0.3	22-24	< 1.5	< 0.5	15-16.5	Bal.	≤0.1	-
Ni-625	< 0.4	< 1.0	20-23	< 5.0	< 0.5	8-10	Bal.	≤0.5	Nb, Ta, Ti
Fe-556	0.2	18	22	Bal	1.0	3	20	0.4	W, Ta, N
Steel-310	-	-	24-26	Bal.	< 2.0	-	19-22	≤1.75	C
Steel-316	-	-	16-18	Bal.	< 2.0	2-3	10-14	≤0.75	-

Table 1. Typical chemical compositions of the metal alloys utilised in this study (% wt).

The wall-end of the main tube was attached to an air compressor, which fed air to the probe at a rate of 37.4 m^3/hr (1320 ft^3/hr) at 4.5 bars. The air flowed freely into the furnace at the other end. The air temperatures inside the probe were measured by three thermocouples and were recorded using a data logger. After approximately 800 hours of exposure to the hot flue gas, which had a temperature range of 730-813°C, each probe was carefully removed, disassembled and analyzed.

2.3 Evaluation of the Combustion Process

2.3.1 Combustion Residues and Probe Deposits

Samples of ash and combustion residue deposits were collected from various locations and subsequently analysed for their properties and composition. Probe deposits, in addition to bottom ash, wall slag, superheater fouling deposits, economiser ash and fabric filter flyash were characterised and the concentration of the elements present were linked to their role in inducing hot corrosion.

2.3.2 Composition and Phase Analysis

Elemental analysis was conducted using a Spectro Genesis – Simultaneous CCD-ICP (Charged Coupled Device – Inductively Coupled Plasma) Spectrometer, a Perkin Elmer 2400 Elemental Analyzer for CHN analysis and a standard titration method for chlorine. The crystalline phase was investigated with a Siemens D500 Reflection Diffractometer (Copper Radiation), operated with $CuK_\alpha1$ and $K_\alpha2$ at 40 kV and 30 mA.

Differential thermal analysis was carried out using a Perkin Elmer – Differential Thermal Analyzer DTA7 (N538-1045). Microstructure analyses were performed with an Environmental Scanning Electron Microscopy – Phillips XL30 ESEM-FEG, operated at 20 keV. Corrosion rates were analysed by a Reichert Jung – Polyvar Microscope. For grain boundary analysis, etchant No. 105 was used.

2.3.3 Mathematical Modelling of Heat Transfer

Computational fluid dynamics modelling using FLUENT code was carried out in order to simulate the flow characteristics and heat transfer inside the furnace and in the region around the air cooled sampling probes. This was also utilised to calculate the heat transfer of the air cooled sampling probe components.

3. RESULTS AND DISCUSSION

3.1 Sampling Probe Temperatures

The average temperatures of the cooling air inside the sampling probes, SP1 and SP2, are outlined in Table 2. As shown, this resulted in an average temperature difference of 84°C between the wall and end sections. The temperature profiles of both probes gradually decreased as time progressed due to deposit accumulation. The experimental data agreed with the modelling results (considered below), hence, the overall conclusions were drawn from both parts of the study.

Average Temperature (°C)	SP1	SP2
Wall Section	93	117
Middle Section	122	110
End Section	175	204
Difference between Wall and End	82	87

Table 2. Average temperatures measured at various locations on sampling probes 1 and 2.

3.2 Sampling Probes after Furnace Exposure

After the probes were removed from the furnace, the scale layers were inspected. As in the study by Kawahara [14], three different scale layers were detected. This scale was composed of: (i) a thick surface layer deposit on the outside; (ii) hard lamella layers of corrosion products or the un-protective oxide layer under the deposit; and (iii) a thin film of dense, powdery corrosion products at the scale-metal interface. The ranges of deposit thickness on the probes were 7-35 mm for SP1, and 16-40 mm for SP2. The deposits on the

probes were thinner at the hotter region (outlet side) and thicker at the wall end, where it was cooler. Molten deposits were detected on SP1 at the thickest deposit covering on the tube and baffles (this agrees with the modelling results). There was no evidence of molten deposits on SP2.

The amount of corrosion products increased with temperature and was also dependent on the alloy. For SP1, the thickness of the corrosion products from the Ni-based alloys (alloys 59 and 625) was less than 1 mm, while those from the Fe-based alloy 556 were notably thicker, up to 2.5 mm. For SP2, corrosion products were present only as a thin film and visible corrosion products were barely detected on the wall and mid sections of the probe. Corrosion products were thicker at the hotter end. Sections of SP2 after the deposits had been removed are presented in Figure 4. Corrosion products under the deposit layer were slightly thinner than those present on the flue gas-exposed side; their thickness plays a vital role in heat transfer. The corrosion products of the Fe-based alloy 556 were highly porous and detachable, and were the thickest among the three alloys. Superheater tubes made from alloy 556 are therefore prone to reduced efficiency.

(a) (b) (c) (d) (e) (f)
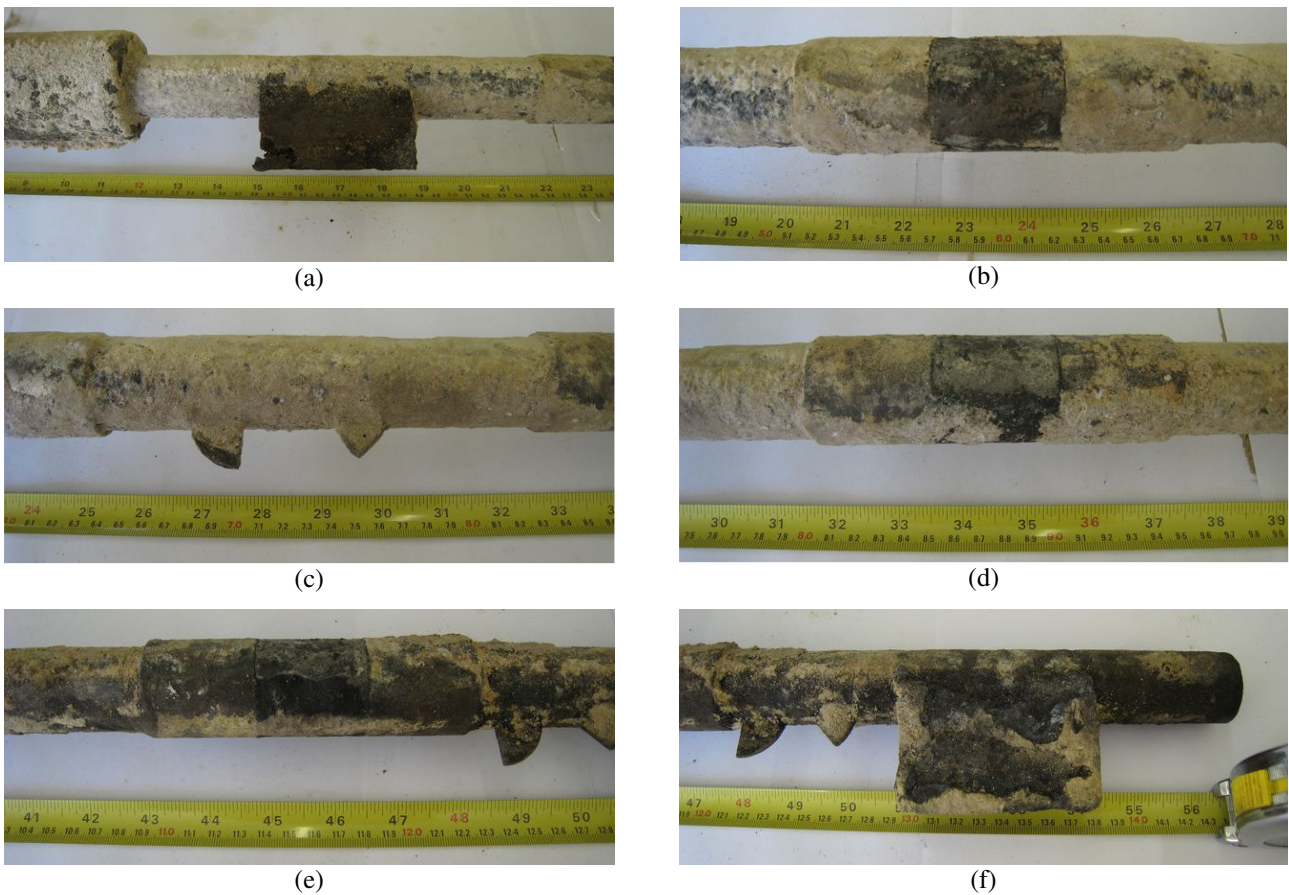
Figure 4. Sampling probe 2 after the deposits were removed: (a) baffle at the wall section; (b) alloy rings at the wall section; (c) coated coupons at the wall section; (d) alloy rings at the mid-section; (e) alloy rings at the end section; and (f) coated coupons and the baffle at the end section.

The baffles were totally covered with deposits and the voids between the baffles and the main tube were also filled with fine yellow particles. The design of these baffles was not found to be beneficial under real operation, as they formed a void for deposit accumulation, where subsequent hot corrosion could take place. Baffles made of stainless steel 316 were severely corroded, leaving brittle dark reddish-brown corrosion products. The edges of the baffles had become chipped and the spallation of corrosion products was common at the edges welded to the main probe. There was no evidence that these baffles could reduce or prevent the corrosion of the 1 inch-tube in the area where they were welded. Instead, it retained the deposits and increased the risk of hot corrosion in that area. The coated coupons were also entirely enclosed by deposits. After the thick deposits were removed, it was found that there was a very thin film of corrosion products randomly formed on the coupon surfaces. There were no chips, broken structures or spallation detected. Both the coated Ni-based alloy 59 and coated stainless steel 310 were found respectively to be in a better condition than the uncoated alloy 59 and comparable materials ferrous (i.e. alloy 556 and stainless steel 316).

3.3 Corrosion Rates of Alloy Rings

The alloy rings (Ni-based alloy 59, Ni-based alloy 625 and Fe-based alloy 556) were analysed for their corrosion rates, where measurements were taken at the cross-sectional surface. The results of these calculated corrosion rates (in mm/year) are plotted against the position on the alloy in Figure 5. The position on the graph directly signifies the real positions on the ring when looked at from the end of the probe. The arrows identify the direction of the flue gas flow that corresponds to the location of the thick deposit layer – the side where the alloys were not directly exposed to the gas flow due to the coverage of the deposits. As shown in both Figure 5 and Table 3, the area covered with the deposit became less corroded than the side exposed to the flue gas because: (i) the thick deposit layer protected the alloy surface from further active oxidation and prevented the volatilization of metal chlorides; and (ii) the thickness of the deposit was able to reduce the surface temperature of the areas it covered. Comparisons of the results from SP1 and SP2 revealed an increase in metal temperature in the former of approximately 50°C (from CFD modelling), which resulted in the identified increase in corrosion rates. The results of the corroded length for the exposure period (µm) and the predicted average corrosion rates are also listed in Table 3. These revealed that the Fe-based alloy 556 had the highest corrosion rate (up to 3.9 mm/yr on SP1) followed by the Ni-based

alloy 59 (up to 3.3 mm/yr). Ni-based alloy 625 had a significantly lower corrosion rate compared to the others (up to 0.5 mm/yr).
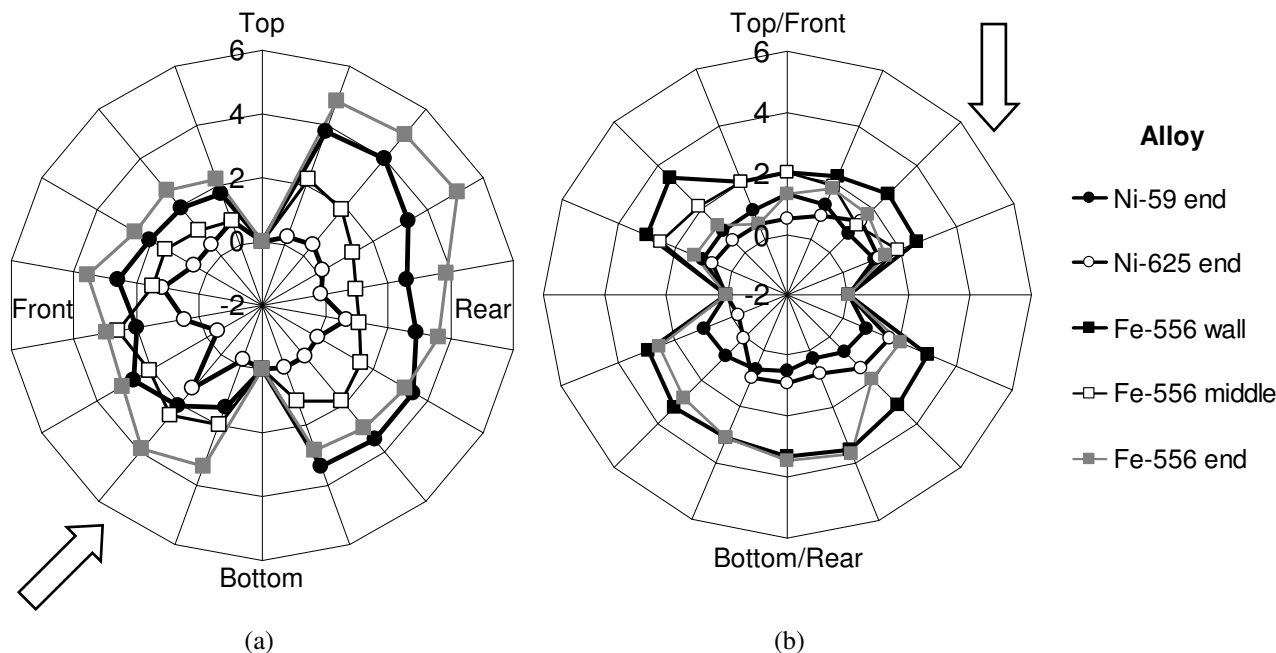
Figure 5. Corrosion rates (mm/year) of alloy rings for (a) sampling probe 1 and (b) sampling probe 2. Arrows show the direction of gas flow.

Alloy Rings		Corrosion of Rings on SP1			Corrosion of Rings on SP2		
		Corroded Length (µm)	Corrosion Rate: Length (mm/yr)	Corrosion Rate: Area (mm^2/yr)	Corroded Length (µm)	Corrosion Rate: Length (mm/yr)	Corrosion Rate: Area (mm^2/yr)
Ni-59 end	F	178.75	2.04	239	104.43	1.13	132
	R	293.62	3.34	387	59.17	0.64	75
Ni-625 end	F	41.27	0.47	53	69.38	0.75	86
	R	14.89	0.17	19	67.87	0.73	86
Fe-556 wall	F	-	-	-	242.28	2.62	300
	R	-	-	-	287.18	3.10	355
Fe-556 mid	F	150.33	1.71	189	175.43	1.89	220
	R	131.99	1.50	176	-	-	-
Fe-556 end	F	267.76	3.05	354	123.86	1.34	155
	R	343.60	3.91	456	240.69	2.60	304

Table 3. Average corroded lengths and corrosion rates of the different alloys on sampling probes 1 and 2, for the front (F) and rear (R).

3.4 Grain Boundaries in Corroded Areas

Etched cross-section images of the grain boundary at the corroded areas of alloy 59, alloy 625 and alloy 556 are shown in Figure 6. The corrosion of the two Ni-based alloys (alloy 59 and alloy 625) took place in a uniform mode at the grain boundaries. Pitting along the grain boundaries of both alloy 59 (Figure 6a) and alloy 625 (Figure 6b) was obvious, but the deeper pits were detected at the surface of alloy59. For the Fe-

based alloy 556, corrosion took place uniformly on the surface and cracking on the grain boundary was not detected (Figure 6c).
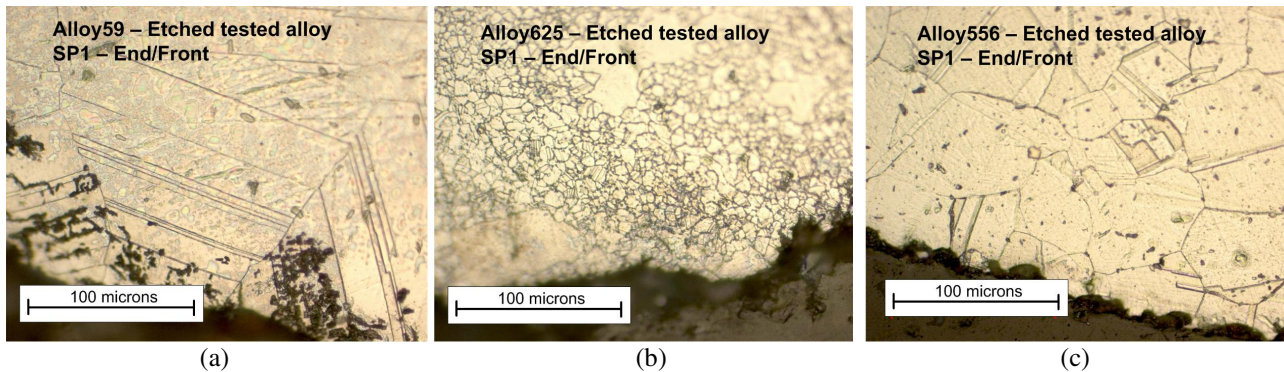
Figure 6. Cross-sectional images and grain boundary structures of (a) nickel-based alloy 59; (b) nickel-based alloy 625; and (c) iron-based alloy 556.

3.5 Morphology and Crystalline Structure Analysis of Corroded Areas

The morphology of the corroded areas from SP1 established that they were rougher and contained more pits and crevices than the alloy surface of SP2, due to the higher surface temperatures. For SP1, the bottom side of the alloy, despite being exposed to hot gas, corroded uniformly. The top side of the alloy, where deposits accumulated, however was attacked by local corrosion, notably chlorine and heavy metal related-corrosion. For example, the average depth of the pits found on alloy 59 under the deposits was up to 100 μm, while they were less than 20 μm on the opposite side. The models of corrosion mechanisms, governing reactions and thermodynamic considerations have been widely discussed in the literature[7,14-16].

3.5.1 Nickel-based Alloy 59

The SEM cross-sectional images created by X-ray elemental mapping from alloy 59 are shown in Figures 7 and 8. It was clear that this alloy experienced severe corrosion. Both deep pits and wide crevices, as illustrated in these figures, were detected in this sample. The scale layer – a combination of deposits and corrosion products – was mainly composed of: (i) compounds of alkali metals, Pb, As and Zn with S, O and Cl; (ii) oxides of substrate alloy elements; and (iii) other components such as SiO_2, compounds of Al, and C particles. Elements from the deposit, such as Cl, S and Pb were often found at the interface between the corrosion products and the metal surface. This established that the oxide layers of Ni, Cr and Mo existing on the top of this deposit were not protective. There was no evidence of a constant protective oxide layer forming at the metal surface. A layer of nickel oxide (NiO), as identified by SEM and XRD, was detected on

the outside of the scale. The oxides of Mo, followed by oxides of Cr were commonly found closer to the scale/substrate interface. Phases of these oxides were not clearly shown in the XRD results, however, they were reported to be $NiCr_2O_4$, Cr_2O_3 and MoO_2 [14, 17]. The location of metal oxides agrees with Kawahara [14], who stated that chlorides of Cr and Mo oxidized to un-protective oxides ($CrCl_2$, $CrCl_3$, $MoCl_3 \rightarrow Cr_2O_3$, MoO_2) more readily than Ni ($NiCl_2 \rightarrow NiO$) at lower partial pressures of O_2.
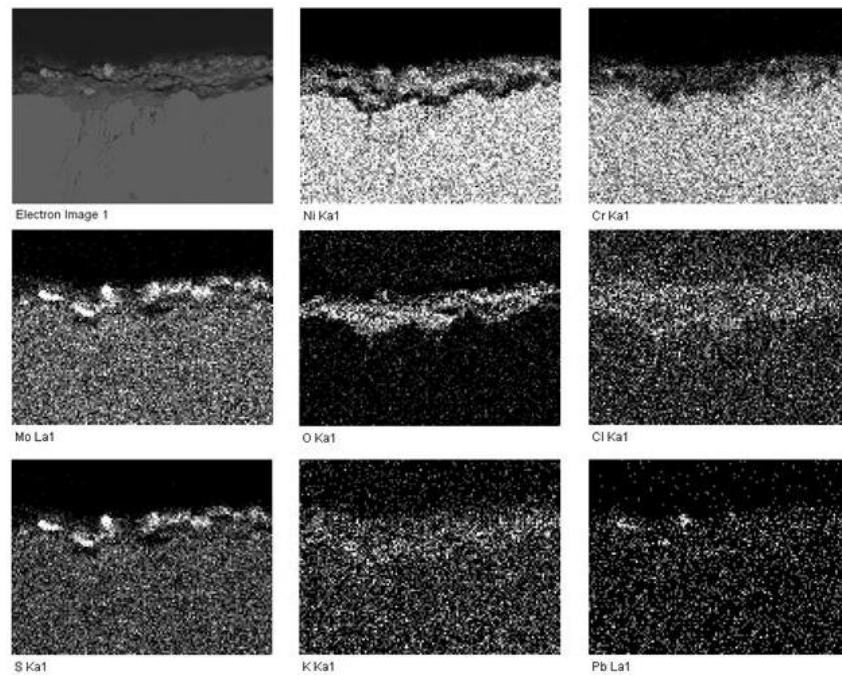
Figure 7. Elemental mapping of nickel-based alloy 59 and its corrosion products at the end of SP1.
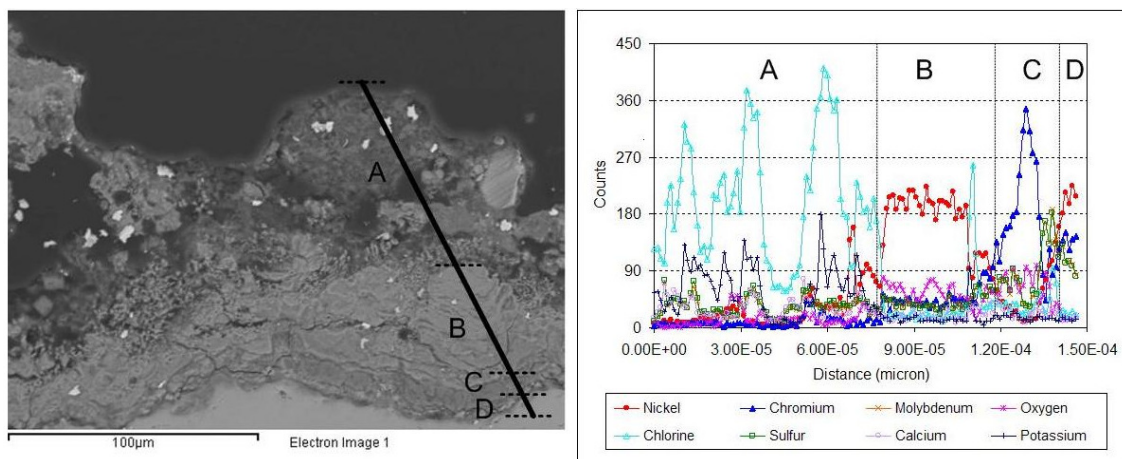
Figure 8. Line scan results of nickel-based alloy 59 at the end of SP1.

3.5.2 Aluminide-Coated Nickel-based Alloy 59

The SEM elemental mapping results for the aluminide-coated coupon of alloy 59 from the wall section is shown in Figure 9 . Results of the crystalline structure analysis from XRD testing are given in Figure 10. It

was found that the scale layers consisted of: (i) deposit layers; (ii) un-protective oxide layers of Al, Ni, Cr, and Mo as θ-Al_2O_3, α-Al_2O_3, NiO, $NiCr_2O_4$, Cr_2O_3, MoO_2 and MoO_3; and (iii) a layer of coating next to the alloy interface. The coating layer was comprised mainly of Al and Ni that were fused to form a Ni-Al inter-metallic layer during the heating process; NiAl, $NiAl_2$ and Ni_2Al_3 were all detected. Figure 11 and Table 4 undoubtedly indicate that the atomic ratios of Ni to Al in this inter-metallic layer varied from 1:1.0 (close to the substrate) to 1:1.4 (top part). A Ni:Al ratio of 1:2.9 was detected in the wall-section coupons. Cr and Mo were also present in the inter-metallic layer but to a lesser extent. Mn was present in the alloy, but its contribution to the protective oxide layer was certainly not demonstrated here.
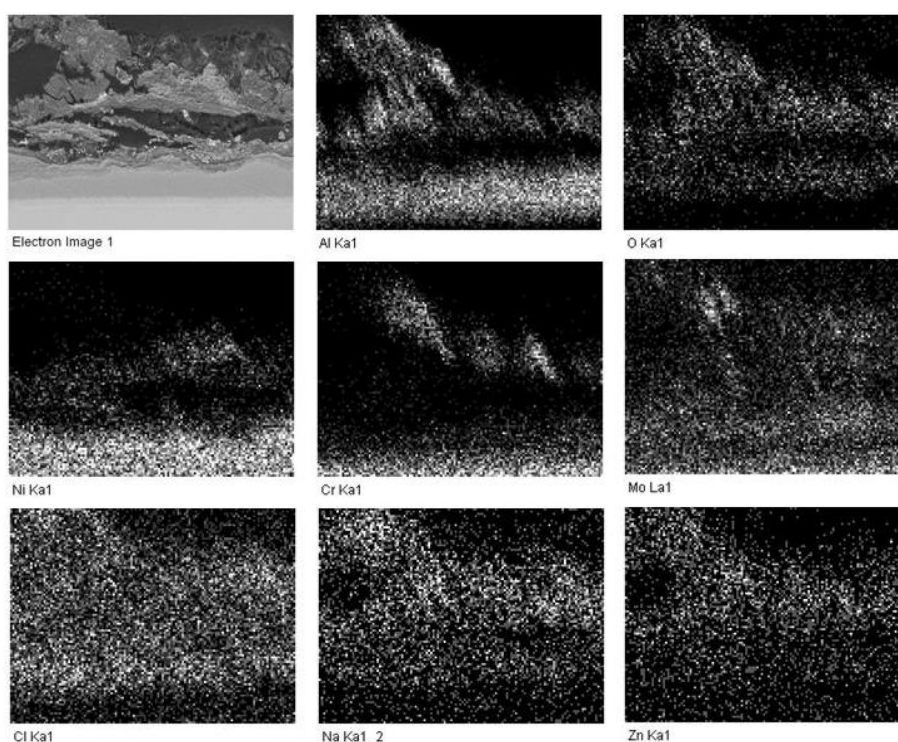
Figure 9. Elemental mapping of aluminide-coated nickel-based alloy 59 and its corrosion products at the wall of SP2.
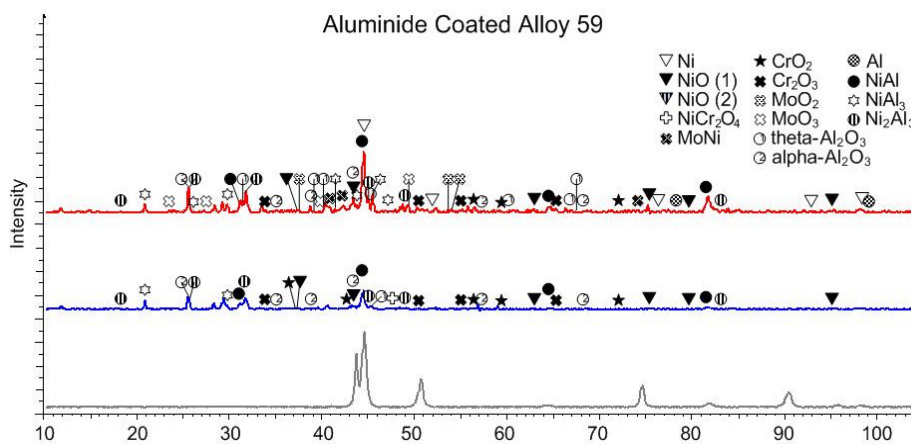
Figure 10. XRD analysis of the aluminide-coated nickel-based alloy 59 on SP2.
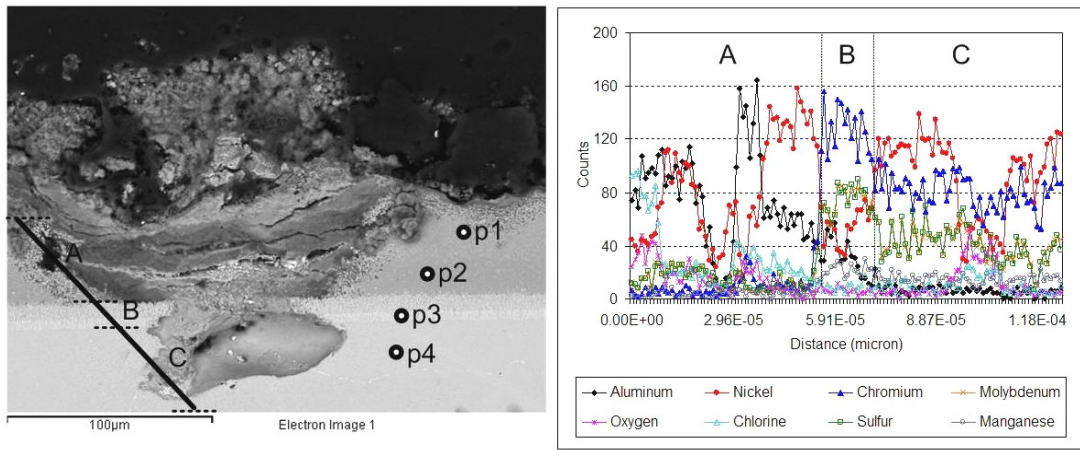
Figure 11. Results of the line scan and point scanning for the end of the aluminide-coated nickel-based alloy 59 on SP2.

Element	Composition – Atomic (%)				Composition – Weight (%)			
	P1	P2	P3	P4	P1	P2	P3	P4
C	45.31	53.26	49.61	47.53	18.83	23.83	16.37	16.18
Al	28.54	22.25	2.08	-	26.65	22.37	1.54	-
Ni	20.03	22.91	21.02	29.74	40.69	50.11	33.90	49.48
Cr	3.95	1.20	19.16	13.09	7.11	2.32	27.37	19.29
Fe	0.33	-	0.57	0.54	0.64	-	0.87	0.86
Mo	1.83	0.38	7.57	4.45	6.09	1.37	19.95	12.09
O	-	-	-	4.65	-	-	-	2.11

Table 4. Elemental composition of the corrosion products at different locations on the end of the aluminide-coated nickel-based alloy 59 on SP2.

Figures 11 and 12 clearly display two different layers of coating above the substrate: (i) a layer of nickel aluminide (region A and Points 1 and 2 on Figure 11, region C on Figure 12); and (ii) a thin layer of Cr next to the substrate (region B and Point 3 on Figure 11, region B on Figure 12). The thickness of the Al-Ni layer at the end- and wall-section coupons were reduced to approximately 60 μm and 70 μm respectively. The thickness of the Cr layer for both coupons was approximately 10-12 μm.
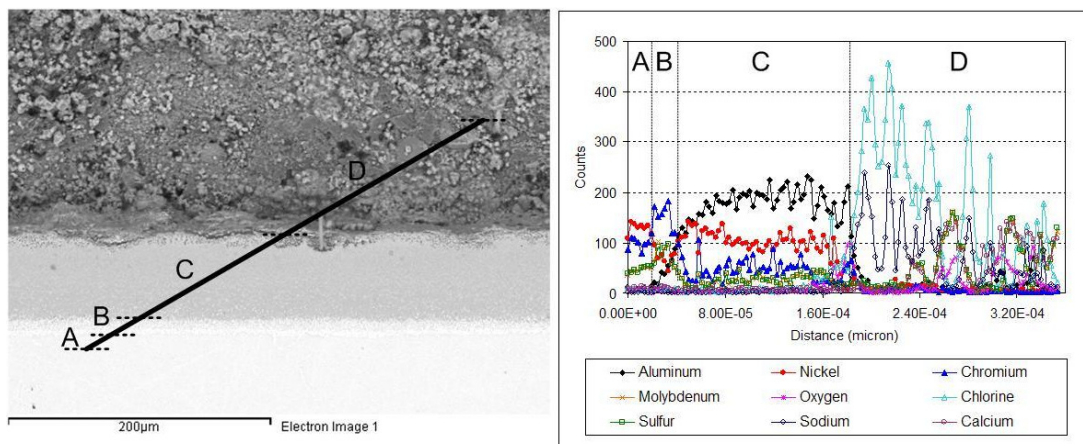
Figure 12. Line scan results of the aluminide-coated nickel-based alloy 59 at the wall-section of SP2.

Images of coated alloy 59 at different locations were compared, as shown in Figure 13. The temperature difference significantly affected corrosion. The cooler wall-section coupon (Figure 13a) was less corroded than the hotter end-section coupon (Figures 13b, 13c and 13d). There was no corrosion at the substrate level on the wall-section, whereas the destruction of the coating and the corrosion of the substrate alloy were widespread in the end-section. The aluminide coating on this Ni-based alloy has proved to be the most efficient method in preventing or at least minimising high-temperature corrosion in the furnace of this WTE plant. The performance of this coating can be enhanced by pre-oxidation prior to exposure to the corrosive gases. Further investigation into the price and strength of the materials are recommended for applications in this field. The drawbacks of NiAl, however, should be carefully considered. These include its insufficient strength, its creep resistance at temperatures above 1000°C, and its brittleness at ambient temperature [12].

(a)

(b)

(c)

(d)
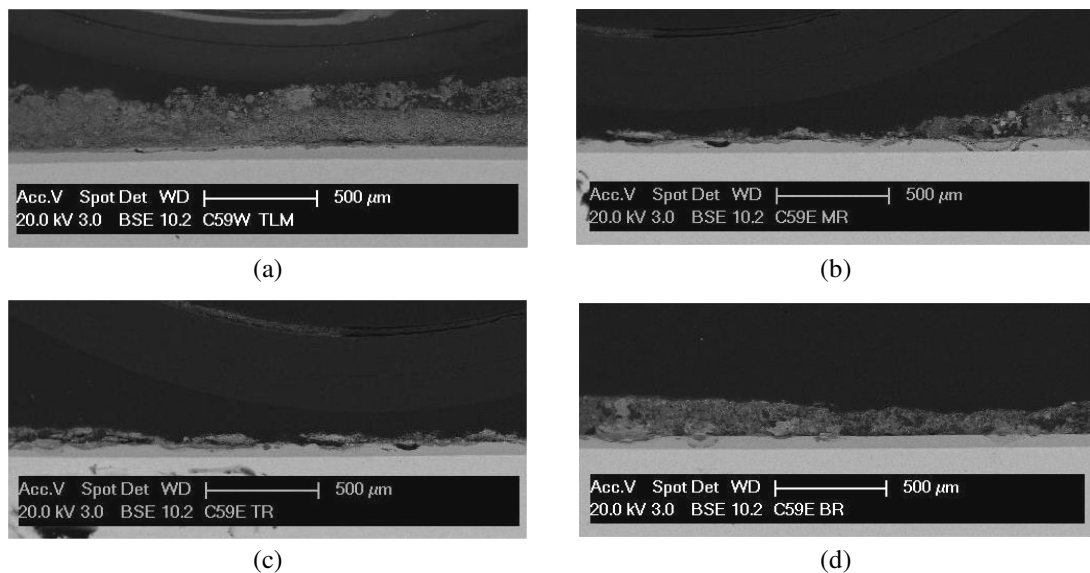
Figure 13. Images of the aluminide-coated nickel-based alloy 59: (a) at the wall-section; and (b), (c) and (d) at the end-section of SP2.

3.5.3 Nickel-based Alloy 625

The elemental mapping and linescan results for the alloy 625 sample are presented in Figures 14 and 15. Analysis of the thick deposit revealed that the very first layer (adjacent to the probe) was often composed of silicon-rich particles, NaCl and KCl. The later deposits contained $CaCl_2$ and $CaSO_4$. Layers of these salts were often detected in between the layers of nickel oxides and chromium/molybdenum oxides. The corrosion products of alloy 625 were similar to that of alloy 59, since they were both Ni-based; oxides of chromium and molybdenum were detected close to the alloy substrate, whereas oxides of nickel were detected in the outer level. The morphology of the corroded areas on alloy 59 and alloy 625 were also

similar. Localized corrosion, such as deep pits and crevices, was frequently noticed, especially on SP1. The corrosion of alloy 625 was however less severe than for alloy 59. The superior performance of alloy 625 compared to alloy 59 may be the result of the lack of Nb, Ta and Ti in alloy 59, as outlined in Table 1. These elements help to protect against the loss of Cr through inter-granular corrosion [18,19]. Results of the crystalline phase study by XRD for alloy 59 and alloy 625 were similar. The corrosion products detected at the alloy surface consisted of NiO, $NiCr_2O_4$, Cr_2O_3, CrO_2, MoO_2 and MoO_3.
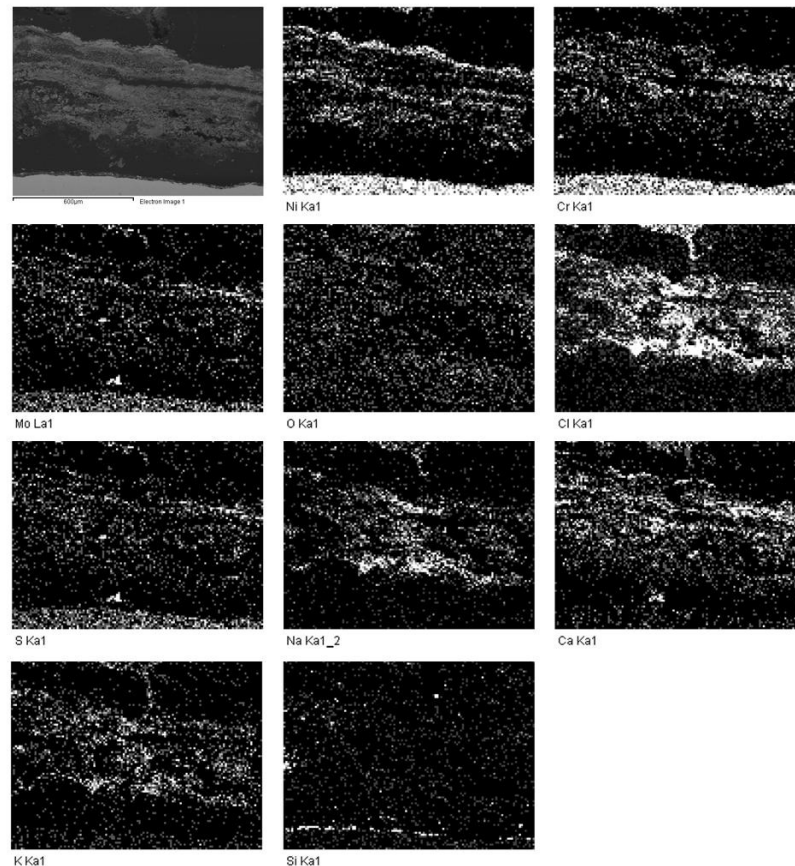
Figure 14. Elemental mapping of nickel-based alloy 625 and its corrosion products at the end of SP1.
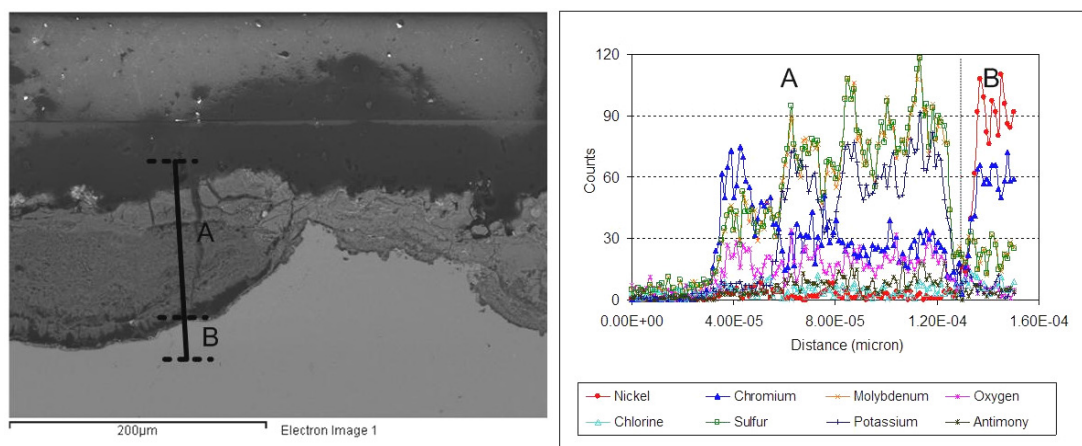
Figure 15. Line scan results for nickel-based alloy 625 at the end of SP2.

3.5.4 Iron-based Alloy 556

The elemental mapping and line scan results for alloy 556 are shown in Figures 16 and 17. The crystalline phases detected on the surface were oxides of iron, nickel and chromium, such as Fe_2O_3, Fe_3O_4, FeO(OH), NiO, Cr_2O_3, CrO_2 and Ni metal. Co was also found in the oxide layers. A layer rich in Cr/Fe was found close to the alloy substrate/scale interface, whereas Co/Ni was found in outer scale. The ability of oxides to prevent the penetration of corrosive deposits was found to be in the following order: $Fe_2O_3 >> Fe_3O_4 > Cr_2O_3 > Al_2O_3 > SiO_2$ [14]. Crevice corrosion and pitting were therefore less likely to occur on the high alloy steel 556. Kawahara [14] also suggested that the stabilities of oxides were in the following order: $Cr > Mo \approx Fe > Ni$ at 500°C. This indicates that the corrosion product layer may form in this order: NiO (on the top), Fe_2O_3 / Fe_3O_4 / MoO_2 and Cr_2O_3 closest to the metal interface. Nevertheless, the stability of chlorides was in the following order: $Cr > Fe > Ni \approx Mo$ at temperatures of 500°C. Alloy 556 was thus more susceptible to corrosion in the chlorine-bearing gas, compared to the Ni-based alloys.
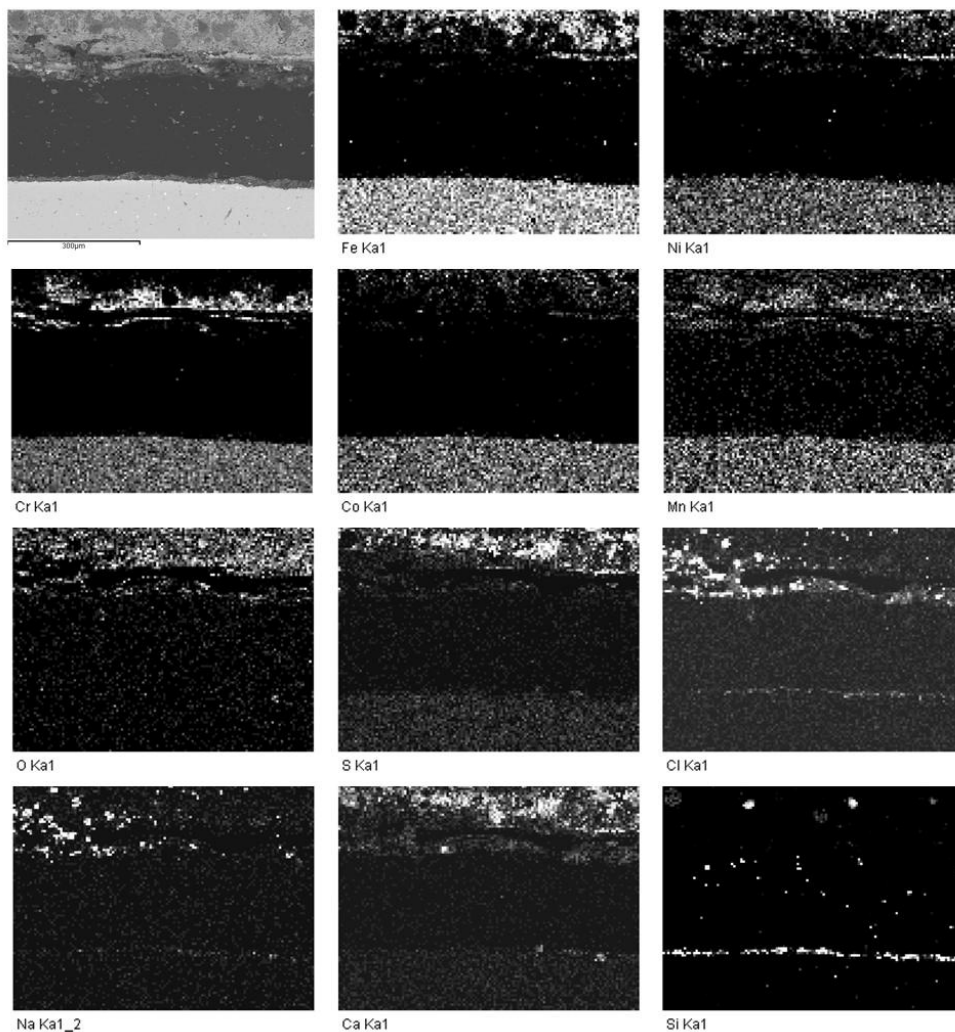
Figure 16. Elemental mapping of iron-based alloy 556 and its corrosion products at the end of SP1.
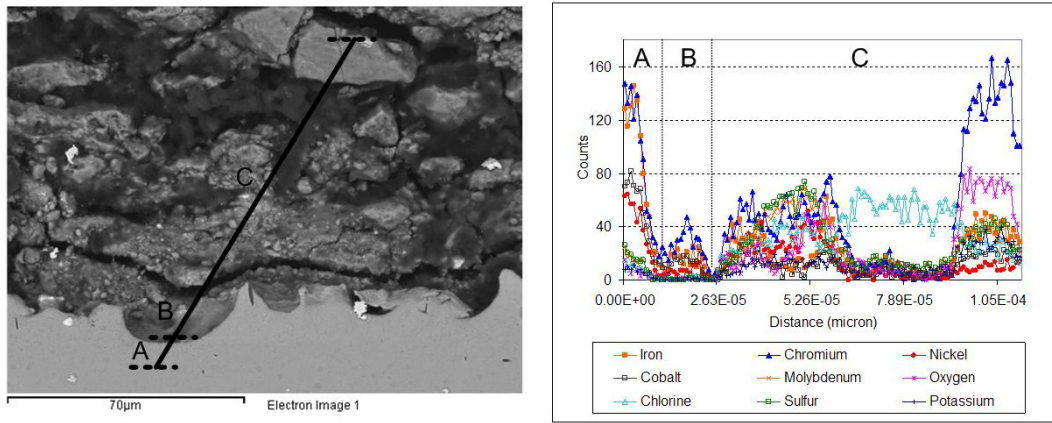
Figure 17. Line scan results for iron-based alloy 556 at the end of SP2.

3.5.5 Aluminide-Coated Stainless Steel 310

The results of the elemental mapping of the aluminide-coated stainless steel coupons are displayed in Figure 18. The coating was barely detected at the end, but remained present at the wall, with a thickness of 3-8 µm. The crystalline structure analysis (Figure 19) revealed that the main components of the corrosion products were θ-Al_2O_3, α-Al_2O_3, Fe_2O_3, Fe_3O_4, FeO(OH), NiO, Cr_2O_3 and CrO_2. The coating layer was a combination of Al and Fe, as FeAl and Fe_3Al inter-metallic compounds. Line scan results for these coupons are shown in Figure 20. The deposit adjacent to this coupon contained high amounts of alkali chlorides. A particle of $CaSiO_4$ was also detected (Figure 20a). Round particles, sized 20-100 μm, were often detected in the deposit, as condensed droplets of liquid $CaCl_2$, $ZnCl_2$, SiO_2 or compounds of Si, Ca, Al, and O. Figures 20b and 20c reveal a thin residual layer of aluminide coating and layers of Al_2O_3 scale present among the deposit.
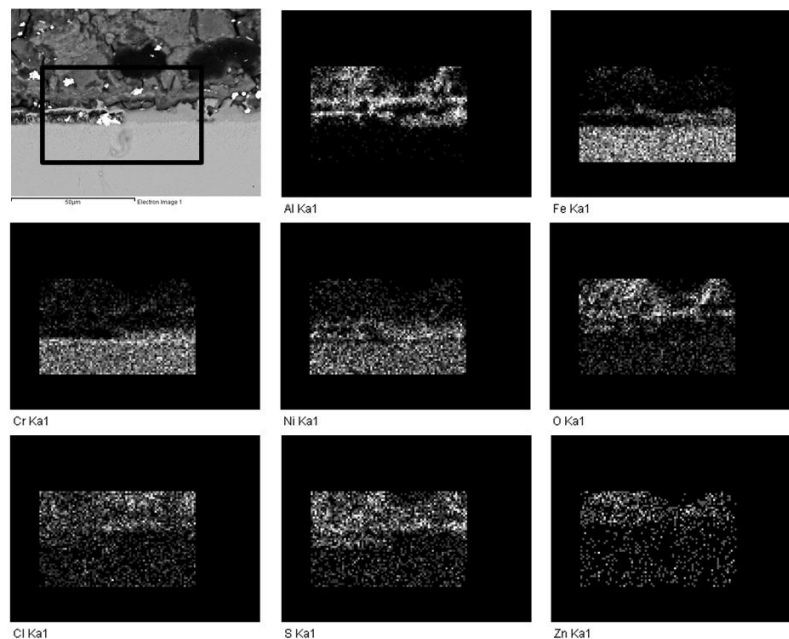
Figure 18. Elemental mapping of aluminide-coated stainless steel 310 and its corrosion products at the wall of SP2.
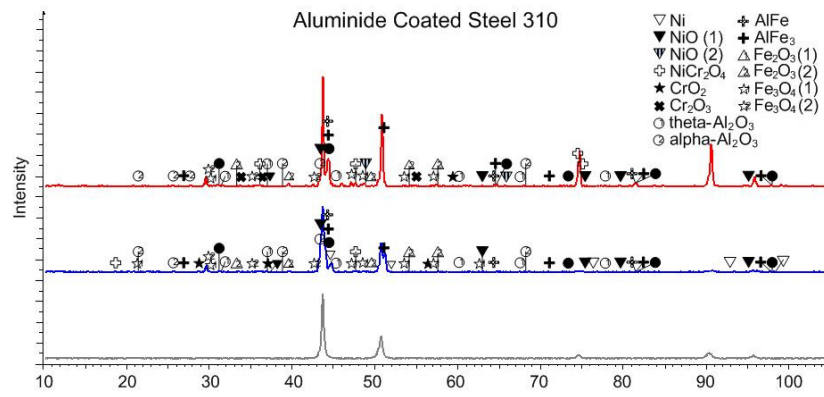
Figure 19. XRD analysis of aluminide-coated stainless steel 310.
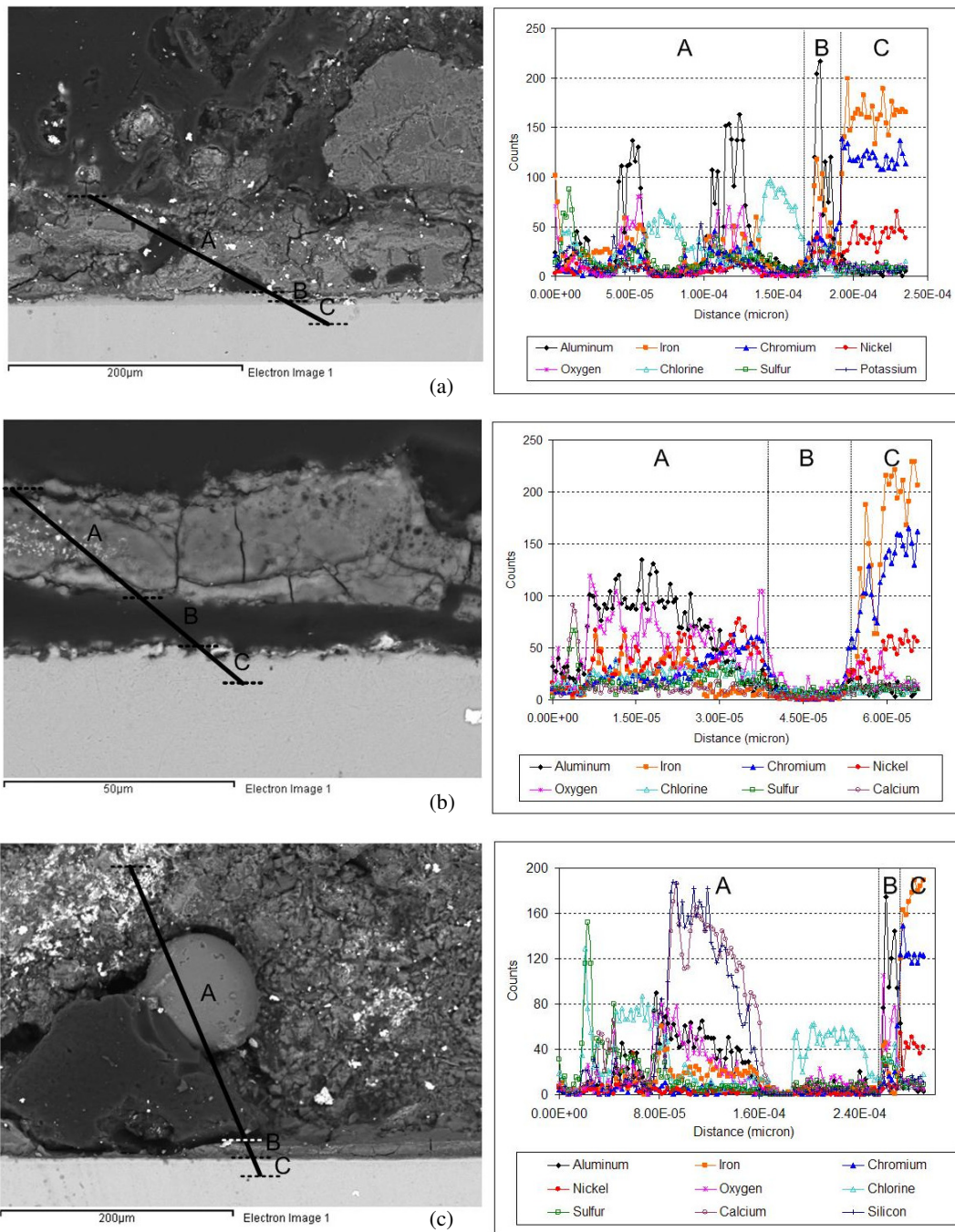
Figure 20. Line scans of the aluminide-coated stainless steel 310 coupons on SP2: (a) and (b) wall; (c) end.

Figure 21 shows the corrosion layer at various positions on the stainless steel 310 coupons. The coating was generally consumed and corrosion reached the substrate level. The coating was detected in the wall-section only at the bottom and middle parts (Figure 21a). It was not found on the top part of the wall-section (Figure 21b) or the end-section (Figures 21c and 21d). This was due to the difference in temperature, the quality of the coating ($FeAl_3$) and the heterogeneous nature of the deposit, causing different rates of localised corrosion.

(a)	(b)
(c)	(d)
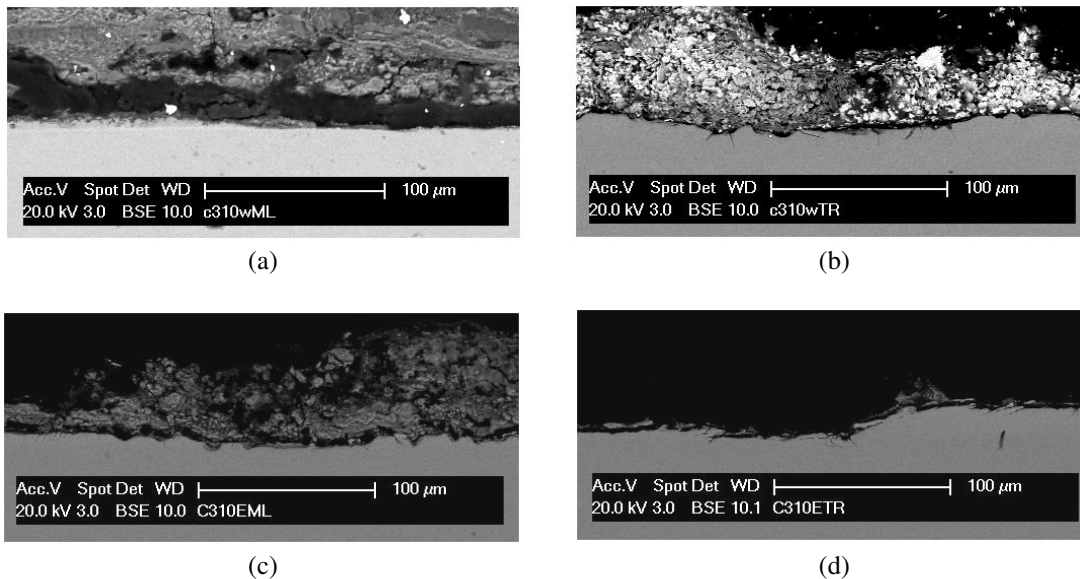
Figure 21. Images of the aluminide-coated stainless steel 310 at (a) the wall; (b), (c) and (d) the end.

In summary, the coated stainless steel 310 established that the aluminide coating can provide good corrosion resistance, if sufficiently thick. The coated coupons suffered less corrosion compared to the uncoated materials, such as stainless steel 316, which was entirely corroded. The aluminide coating on stainless steel did not perform as well as the coating on the Ni-based alloy. These results agreed with previous studies in a laboratory furnace, proving that Al-Fe compounds are less suitable than Al-Ni compounds in a chlorine-bearing, oxidizing environment [13]. Nevertheless, the aluminized coating on the stainless steel had a greater resistance to hot corrosion, compared to the uncoated Ni-based alloys (alloy 59 and alloy 625). It is therefore a promising and cost-effective alternative material to withstand corrosion under such conditions. The additional advantages include the high-temperature strength of the substrate (stainless steel 310) and its low density. The drawbacks on the other hand are the decreasing strength of $AlFe_3$ at temperatures greater than 500°C, the inherent brittleness of the coating at ambient temperature and the susceptibility to chloride attack in high temperature environments [12].

3.5.6 Results for the Stainless Steel 316 Sacrificial Baffles

The baffles made from austenitic stainless steel 316 were found to be severely corroded. SEM results show that the entire baffles were oxidized, which indicates that this material was unable to withstand the corrosive conditions in this high-temperature furnace. The important factor that increased corrosion was the temperature, as the baffles did not have enough surface area for heat transfer to the air cooled probes, and therefore was preferably influenced by the temperature of the surrounding deposits. Corrosion products consisted mainly of Cr_2O_3, Fe_3O_4 and NiO, where oxides of Cr were found close to the substrate and oxides of Fe and Ni were detected in the outer layers.

3.6 Characterisation of Combustion Residues and Probe Deposits

3.6.1 Combustion Residues

Combustion residue samples were collected from various locations inside the furnace. The results specified that the major constituents of the bottom ash were Ca (15.2%), Fe (4.4%), Al (3.4%) and P (1.3%). Samples of wall slag and superheater fouling deposits were composed mainly of Cl (5.45-15.5%), Ca (2.8-14.7%), S (2.2-9.2%), K (3.3-9.0%), Na (1.7-6.2%), Pb (2.5-5.5%), Zn (1.0-3.6%) and Al (1.3-3.1%). High concentrations of Fe (4.3-23.5%) were detected in both the superheater fouling deposits and the economizer ash, most likely derived from the iron oxide layers of the corroded superheater tube surfaces. The air pollution control residue collected by the fabric filter was a mixture of flyash, lime and activated carbon and thus, the major constituents were Ca (19.7%), S (14.8%), and Cl (6.0%); flyash from the economizer ash bunker had a significant and similar proportion of Ca (~20%). Other constituent that were not analyzed in this study were O and Si. Wiles [20] reported the range of Si concentrations to be 9.1-31% for bottom ash, 9.5-21% for flyash and 3.6-12% for air pollution control residues. The common inorganic compounds in flyash collected from WTE plants have been reported in other studies [21].

3.6.2 Probe Deposits

The major elements in the deposits on both probes were relatively similar to those of the surrounding areas. The elemental composition of the deposits on SP1 and SP2 are outlined in Table 5, along with the major constituents from the superheater deposits. The major elements found were Cl (9.1-27.3%), Ca (13.8-23.6%), K (2.0-11.4%), Na (2.1-8.6%), S (4.2-7.1%) and Al (1.0-3.1%). These elements, combined with heavy metals, such as Zn (up to 1.0%), Pb (up to 0.23%), Cd (up to 0.3%) and Sn (up to 0.03%) signify that

there is the potential for low-melting point-compounds to form, which could induce severe hot corrosion [22]. Ca and Cl were detected more in the probe deposits compared to slag samples, because the lower surface temperatures of the probes can induce more particle deposition. These deposits were also analysed by DTA. The results showed that some components of the superheater deposit could possibly melt at temperatures as low as 272°C. This melting temperature could be of eutectic compounds or binary mixtures, comprised of Cl [15, 23]. The general melting temperatures for these deposits, however, were in the range of 524-683°C, which are similar to those of Kawahara [14], who reported melting temperatures of 484-555°C.

	Deposit from Sampling Probe 1 (wt%)				Deposit from Sampling Probe 2 (wt%)				Superheater (wt%)	
	Wall	Middle	End 1	End 2	Wall	Middle	End 1	End 2	Deposit 1	Deposit 2
Al	1.37	1.57	1.73	2.37	1.80	1.40	1.60	1.00	0.36	1.29
Ca	17.60	18.10	14.60	22.40	20.10	16.50	16.80	13.80	2.85	9.80
Cl	15.99	27.31	n.m.	9.09	12.72	19.98	18.65	23.26	11.10	5.45
Fe	0.45	0.46	0.75	0.74	0.64	0.52	0.59	0.33	23.50	4.32
K	8.32	9.09	8.55	3.22	4.92	8.70	8.45	11.40	3.31	8.19
Mg	0.72	0.82	0.80	1.20	0.78	0.60	0.64	0.41	0.14	0.53
Na	6.62	6.90	6.6	3.09	4.34	6.48	6.30	8.60	2.27	6.05
Ni	0.05	0.00	2.27	0.08	0.03	0.00	0.11	0.00	-	-
Pb	0.14	0.11	0.23	0.03	0.10	0.11	0.13	0.11	-	-
S	5.08	5.37	4.24	4.93	6.00	6.50	6.10	7.10	2.60	7.57
Zn	0.59	0.83	1.02	0.46	0.51	0.76	0.81	0.66	1.09	2.02

Table 5. Major elemental composition of the deposits collected from SP1, SP2 and the superheater.
Note: n.m. is 'not measured'

3.6.3 Detached Corrosion Products

The elemental composition of the corrosion products detached from the alloys was a combination of the deposit and the elements from the alloys. The major components of the corroded elements for the Ni-based alloys (alloy 59 and alloy 625) were Ni (6.7-8.4%), Cr (1.4-1.8%) and Mo (1.0-2.2%). Fe (5.7-7.8%), Ni (4.0-5.3%), Cr (2.5-3.5%) and Co (2.8-3.6%) were abundant in the corrosion products of the Fe-based alloy 556. For stainless steel 316, Ni (1.4-1.5%) and Fe (about 1.5%) were the key elements. Large amounts of Zn (1.3-3.0%), Pb (up to 3.4%) and Cd (up to 0.14%) were also noted in these corrosion products.

3.7 Mathematical Modelling

The modelling results for velocity vectors and temperature contours of the combustion gas stream in the furnace and superheater (Figure 22) corresponded relatively well to the values recorded by probes at the plant (Table 6). The simulations demonstrated that the conditions in the furnace were oxidizing (6.8% O_2), with the presence of steam (17.7% H_2O), which is a favourable environment for high-temperature corrosion.

<p style="text-align:center">(a)</p>
<p style="text-align:center">(b)</p>
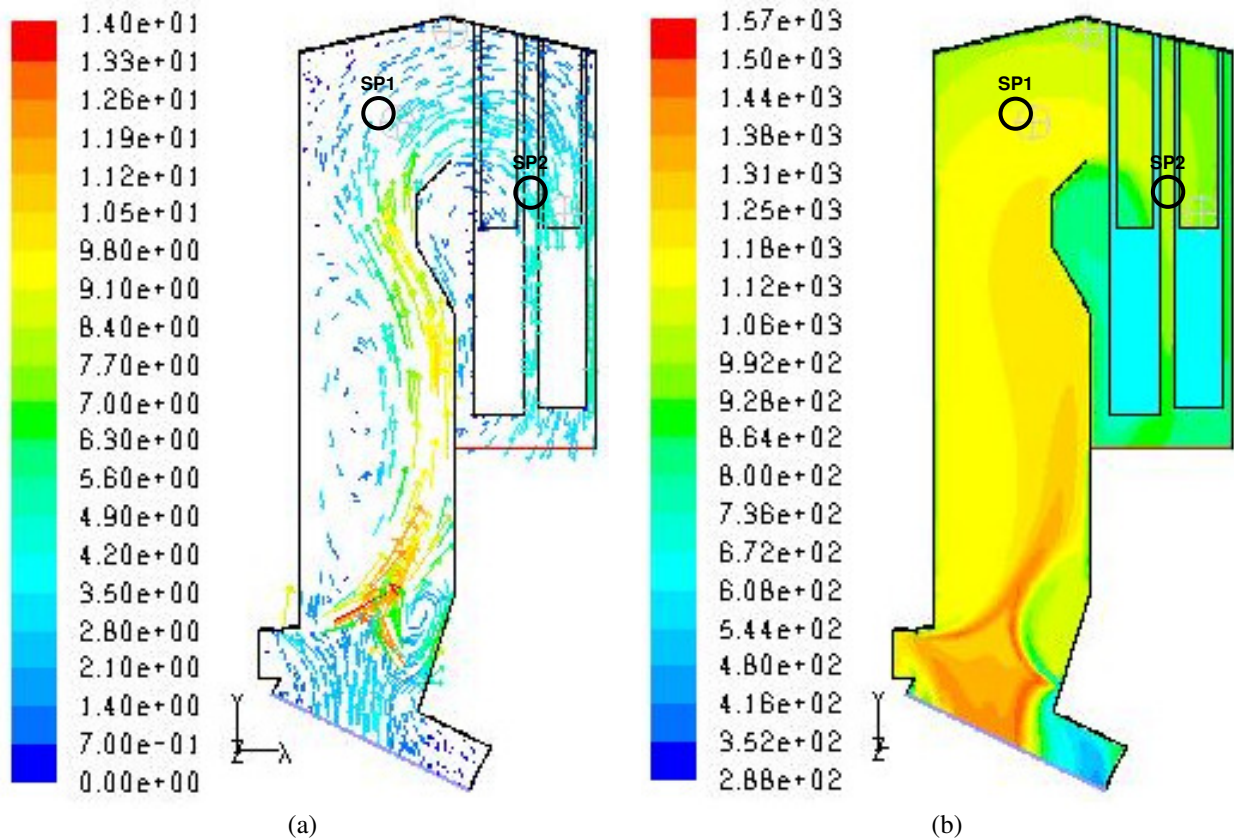
Figure 22. The modelled furnace and superheaters, showing (a) the gas velocity vectors by magnitude (m/s); and (b) gas temperature contours (K). The locations of the sampling probes (SP1 and SP2) are also identified.

	Results	Real Measurement	Model
Temperature (°C)	roof probe	804-828	769
	1st pass/Probe SP1	754-813	871
	2nd pass/Probe SP2	730-791	717
Velocity (m/s)	roof probe	-	1.26
	1st pass/Probe SP1	-	3.05 (X =2.02,Y=2.28,θ = -138.4°)
	2nd pass/Probe SP2	≈ 5	4.83 (X = 0.41, Y=-4.81, θ= 4.83°)
O_2 content (wt%)	roof probe	-	6.55
	1st pass/Probe SP1	8.38-8.77	6.69
	2nd pass/Probe SP2	-	6.68

Table 6. Comparison of the results from the FLUENT modelling and the on-line recorded values.

The modelling results for the velocity vectors and the temperature profile for the sampling probes are shown in Figures 23 and 24; similar results were found for SP1 and SP2. The surface temperatures of the alloy rings and the deposit on the probes are outlined in Table 7. The results in Figure 24 illustrate that the surface temperatures of the alloy rings on the probes were in the range of 404-495°C for SP1 and 363-440°C for SP2. The surface temperatures of the deposits could however be as high as 680°C. This calculation supports the experimental findings, that hot corrosion took place under the deposits on SP1. The modelling identified

that the coated coupons found under the deposit could be entirely surrounded by the hot deposits, having temperatures of up to 615°C; this means that these coupons experienced higher surface temperatures than the alloy rings on the probes.
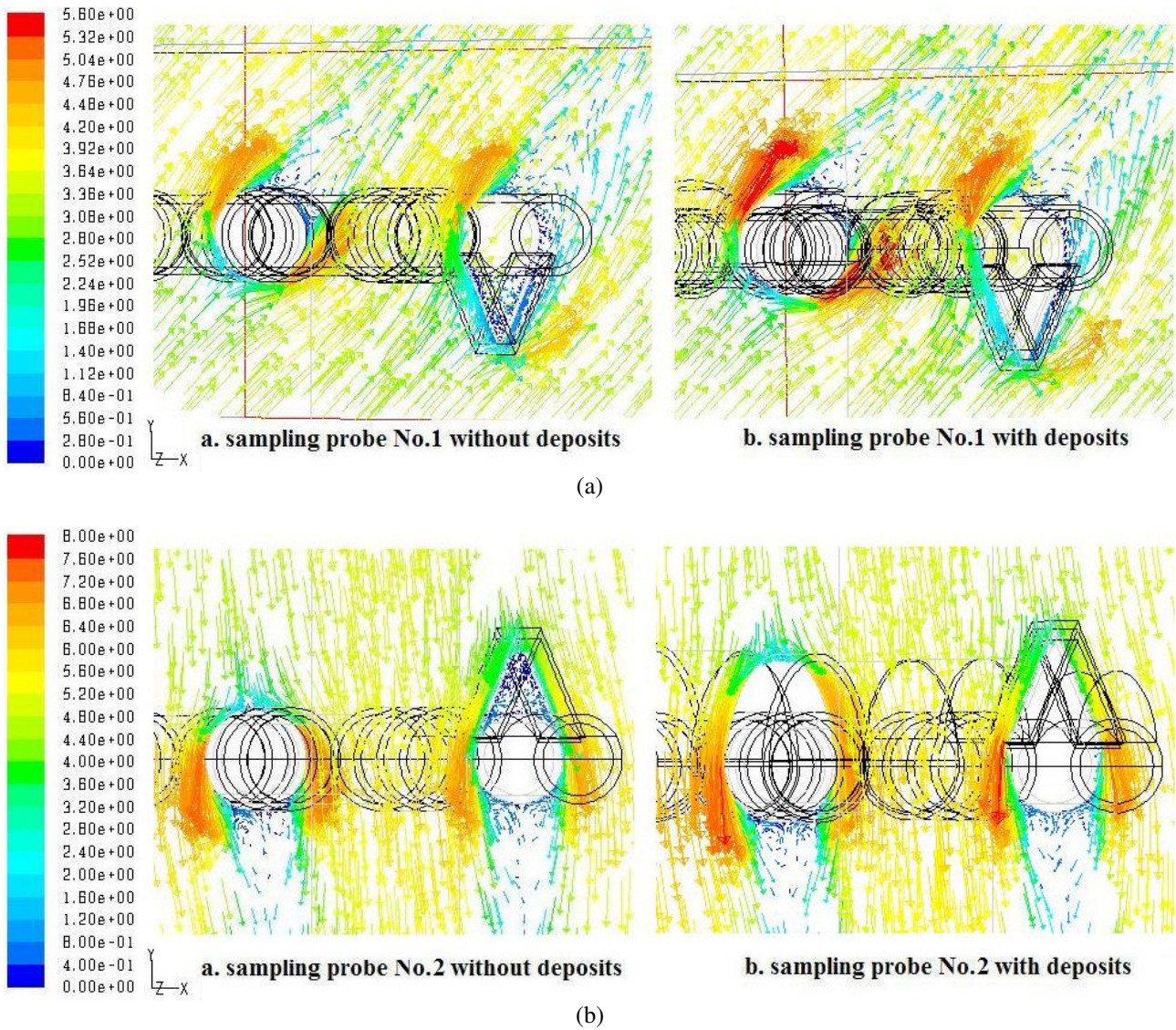
Figure 23. Modelled velocity vectors by magnitude (m/s), of the flow across (a) SP1 and (b) SP2.

The 2D modelling work revealed that baffles could divert the particles from the probe, preventing deposition and erosion corrosion. The temperature of the baffle itself, however, was very high, since the heat transfer surface connected with the main tube was very small. The installation of the baffle, by welding it to the main tube, increased the local surface temperatures of the main tube by approximately 1.74%. This finding raises concern about the use of sacrificial baffles in the industry. The welding points possibly become the source of localized corrosion, which can potentially puncture the superheater tubes.

(a)

(b)
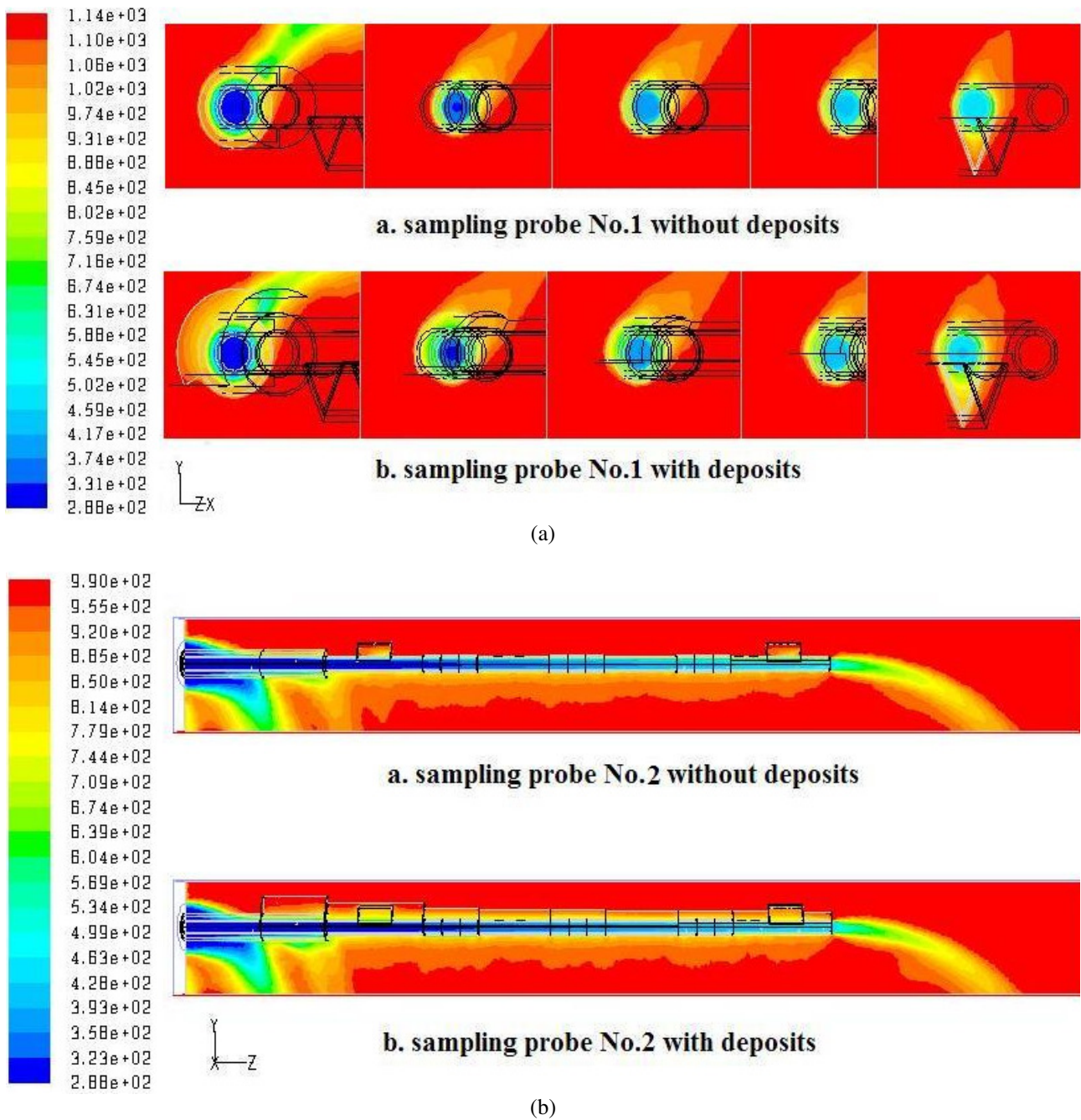
Figure 24. Modelled temperature contours (K) with and without deposits: (a) at various cross-sections of SP1 and (b) of SP2.

Surface Temperature (°C)	Location (section)	Sampling Probe 1		Sampling Probe 2	
		No deposits	With deposits	No deposits	With deposits
Metal Surface Temperature	0.59 m (wall)	452-496	404-427	397-434	363-378
	0.87 m (mid)	477-518	435-462	419-453	385-401
	1.15 m (end)	504-543	468-495	441-474	418-440
Deposit Surface Temperature	0.59 m (wall)		489-680		399-598
	0.87 m (mid)	n.a.	514-641	n.a.	419-596
	1.15 m (end)		542-631		615

Table 7. Surface temperatures (°C) of the metal and deposits at different locations on the sampling probes.

4. CONCLUSIONS

The results from this study have yielded valuable information that can be applied to the waste-to-energy industry or those that have similarly corrosive environments. Both temperature and deposits greatly influenced corrosion rates. The higher temperature region experienced severe deposit-induced corrosion or hot corrosion, where the melting temperature of the deposits was 524-683°C. A thick deposit could decrease corrosion rates by reducing surface temperatures, protecting it from further active oxidation and preventing the volatilization of metal chlorides. However, this is valid only if the deposit has not melted. The nickel-based alloys had lower corrosion rates than the iron-based alloy. They were however more prone to localized corrosion, most notably from alkali-metal chlorides, and had a lower resistance against pits and crevices.

The use of an aluminide coating, which is relatively cheap and simple, could act as a promising corrosion control technique for superheater materials. The order of corrosion resistance for the materials and coatings tested was: aluminide-coated nickel-based alloy 59 > aluminide-coated stainless steel 310 > nickel-based alloy 625 > nickel-based alloy 59 > iron-based alloy 556 > stainless steel 316. The hot corrosion resistance of FeAl and Fe_3Al formed on the low-cost stainless steel 310 is comparable to that of more expensive nickel-based alloys, although the chloridation resistance is not particularly high, due to the relatively low nickel content in the steel. Furthermore, the results demonstrated that sacrificial baffles tend to promote deposit accumulation and therefore cause higher temperatures at the welding points. As a result, deposit-induced corrosion can take place more vigorously.

ACKNOWLEDGEMENTS

REFERENCES

[1] F.J. Frandsen, Utilizing biomass and waste for power production – A decade of contributing to the understanding, interpretation and analysis of deposits and corrosion products, *Fuel* 84 (2005), 1277-1294.

[2] K. Persson, M. Broström, J. Carlsson, A. Nordin, R. Backman, High temperature corrosion in a 65 MW waste to energy plant, *Fuel Process. Technol.* 88 (2007), 1178-1182.

[3] S. Srikanth, B. Ravikumar, S.K. Das, K. Gopalakrishna, K. Nandakumar, P. Vijayan, Analysis of failures in boiler tubes due to fireside corrosion in a waste heat recovery boiler, *Eng. Failure Anal.* 10 (2003), 59-66.

[4] R. Streiff, J. Stringer, R.C. Krutenat, M. Caillet, *High Temperature Corrosion of Materials and Coatings for Energy Systems and Turboengines* (1987), Essex England: Elsevier Applied Science Publishers Ltd.

[5] R.A. Rapp, J.H. Devan, D.L. Douglass, P.C. Nordine, F.S. Petit, D.P. Whittle, High temperature corrosion in energy systems, *Mater. Sci. Eng.* 50 (1981), 1-17.

[6] T.S. Sidhu, R.D. Agrawal, S. Prakash, Hot corrosion of some superalloys and role of high-velocity oxy-fuel spray coatings – A review, *Surf. Coat. Technol.* 198 (2005), 441-446.

[7] T. Ishitsuka, K. Nose, Stability of protective oxide films in waste incineration environment – solubility measurement of oxides in molten chlorides, *Corros. Sci.* 44 (2002), 247-263.

[8] J. Swithenbank, V. Nasserzadeh, A. Wasantakorn, P.H. Lee, C. Swithenbank, Future integrated waste, energy and pollution management (WEP) systems exploit pyrotechnology, *Process Saf. Environ. Prot.* 78 (2000), 383-398.

[9] L.A. Hansen, H.P. Nielsen, F.J. Frandsen, K. Dam-Johansen, S. Horlyck, A. Karlsson, Influence of deposit formation on corrosion at a straw-fired boiler, *Fuel Process. Technol.* 64 (2000), 189-209.

[10] Y.S. Li, Y. Niu, W.T. Wu, Accelerated corrosion of pure Fe, Ni, Cr and several Fe-based alloys induced by $ZnCl_2$-KCl at 450°C in oxidizing environment, *Mater. Sci. Eng.* A 345 (2003), 64-71.

[11] J.L. He, C.H. Yu, A. Leyland, A.D. Wilson, A. Matthews, A comparative study of the cyclic thermal oxidation of PVD nickel aluminide coatings, *Surf. Coat. Technol.* 155 (2002), 67-79.

[12] C. Houngninou, S. Chevalier, J.P. Larpin, Synthesis and characterisation of pack cemented aluminide coatings on metals, *Appl. Surf. Sci.* 236 (2004), 256-269.

[13] C.C. Tsaur, J.C. Rock, Y.Y. Chang, The effect of NaCl deposit and thermal cycle on an aluminide layer coated on 310 stainless steel, *Mater. Chem. Phys.* 91 (2005), 330-337.

[14] Y. Kawahara, High temperature corrosion mechanisms and effect of alloying elements for materials used in waste incineration environment, *Corros. Sci.* 44 (2002), 223-245.

[15] H.P. Nielsen, F.J. Frandsen, K. Dam-Johansen, L.L. Baxter, The implications of chlorine-associated corrosion on the operation of biomass-fired boilers, *Prog. Energy Combust. Sci.* 26 (2000), 283-298.

[16] A. Zahs, M. Spiegel, H.J. Grabke, Chloridation and oxidation of iron, chromium, nickel and their alloys in chloridizing and oxidizing atmospheres at 400-700 °C, *Corros. Sci.* 42 (2000), 1093-1122.

[17] S. Zhao, X. Xishan, G.D. Smith, S.J. Patel, The corrosion of INCONEL alloy 740 in simulated environments for pulverized coal-fired boiler, *Mater. Chem. Phys.* 90 (2005), 275-281.

[18] W.D. Callister, *Materials Science and Engineering: An Introduction*, 7th edn., (2007) New York: John Wiley & Sons, Inc.

[19] P.A. Schweitzer, *Fundamentals of Metallic Corrosion: Atmospheric and Media Corrosion of Metals*, 2nd edn., (2007) Florida: CRS Press (Taylor & Francis Group).

[20] C.C. Wiles, Municipal solid waste combustion ash: State-of-the-knowledge, *J. Hazard. Mater.* 47 (1996), 325-344.

[21] S.V. Vassilev, C. Braekman-Danheux, Characterization of refuse-derived char from municipal solid waste: 2. Occurrence, abundance and source of trace elements, *Fuel Process. Technol.* 59 (1999), 135-161.

[22] M.A. Uusitalo, P.M.J. Vuoristo, T.A. Mantyla, High temperature corrosion of coatings and boiler steels below chlorine-containing salt deposits, *Corros. Sci.* 46 (2004), 1311-1331.

[23] P. Rademakers, W. Hesseling, J. van der Wetering, *Review on Corrosion in Waste Incinerators, and Possible Effect of Bromine* (2002) TNO Industrial Technology. Report No. I02/01333/RAD CEF-12.

Abbreviations

CFD　　　　Computational fluid dynamics

MSW　　　　Municipal solid waste

SEM　　　　Scanning electron microscopy

SP1　　　　Sampling probe 1

SP2　　　　Sampling probe 2

WTE　　　　Waste-to-energy